Fingertip-Powered Interactive Gaming: A Sustainable Approach to Human-Machine Interaction

Xin Li, *Member, IEEE*, Yuxing Zhong, *Student Member, IEEE*, Xinyuan Chuai, Yaoyi Li, Weifeng Huang, Jiaming Chen, Xinming Zhang, Daxing Zhang, Congsi Wang, Guobiao Hu, *Member, IEEE*, Junrui Liang, *Senior Member, IEEE*, and Wei-Hsin Liao, *Senior Member, IEEE*

***Abstract*—Human-motion energy harvesting is emerging as a promising solution for wearable electronics and devices, offering a sustainable power source that extends operational longevity and enhances durability. However, current techniques and prototypes have yet to achieve fully interactive, battery-free functionality. This paper presents a battery-free interactive gaming system powered by energy harvested from transient fingertip motion. To ensure the reactivity, interactivity, and stability of the fingertip motion harvester (FMH), we employ a multistable structure. The FMH unit provides a reliable energy solution by utilizing pre-charged potential energy within dynamically varying potential wells. Additionally, the integration of a bistable screen design facilitates seamless gaming experiences, decouples game logic from user interface mechanics, and ensures rapid system recovery after power interruptions. Beyond advancing fundamental research, this work pioneers a practical battery-free interaction paradigm based on fingertip motion, with potential for broader battery-free user interfaces and low-power interactive systems.**

***Index Terms*—Battery-free IoT, Vibration/kinetic energy harvesting.**

I. Introduction

THE emergence of human-motion energy harvesters has spurred interest in replacing conventional batteries for smart electronics [1]. Leveraging ubiquitous, renewable motion, these systems promise clean, fit-and-forget power for portable and wearable devices [2], [3]. Practical outputs primarily come from everyday activities such as walking, running, and typing, which deliver useful power with minimal user burden [4]. Representative implementations include footstep harvesters using sole/insole mechanisms that transfer vertical loading and convert linear displacement to rotational drive via gearing [5], [6], [7], [8]. Limb-swing and joint-rotation devices, including rope-driven rotors, cycloidal electromagnetic generators, and orthosis-integrated knee harvesters, extend coverage across walking and running [9], [10]. At the wearable scale, watch-grade generators such as frequency-up-converted coaxial designs and compact electret harvesters demonstrate practical integration with improved conversion efficiency [11], [12], [13].

However, when tasks shift from low-duty-cycle, fault-tolerant sampling to strongly interactive human–computer loops, a clear quality of service (QoS) gap remains relative to battery-powered devices [22], [23], [24]. On the one hand, the energy available from piezoelectric, electromagnetic, or triboelectric transducers is far below the demands of consumer electronics such as smartwatches and interactive screens [25], [26], [27]. Even kinetic-powered watches can briefly reach milliwatt-level outputs during active use, yet over a day they typically accumulate less than 1% of the energy stored in embedded lithium-ion batteries [28], [29]. On the other hand, the harvested supply is intrinsically unstable due to the intermittent, irregular, and unpredictable nature of human motion, which leads to power interruptions, device restarts, and degraded user experience [30], [31]. Moreover, strongly interactive workloads require per-action atomic completion within a bounded time window, where a single press must cover resume and compute, transactional checkpointing, and a visually consistent display update [32], [33].

Fingertip motion is a fine-grained, controllable energy source that matches the temporal and force characteristics of common human-machine interactions. As summarized in Table I, keystroke impacts can be transduced into electrical outputs and self-sensing signals, enabling energy harvesting and interaction inference on the same hardware. Triboelectric nanogenerator (TENG) keyboards demonstrate this capability [14], [15], but key-scale output remains limited. For example, Li et al. [15] report 0.8 mJ over one hour at 6 Hz. Subsequent studies investigated key-level electromagnetic mechanisms, including electromagnetic buttons (EM buttons) with TENG + EM

Received 28 September 2025; accepted 21 November 2025. Date of publication 5 December 2025; date of current version 6 April 2026. This work was supported in part by the Guangdong Basic and Applied Basic Research Foundation under Grant 2025A1515011342, in part by Hong Kong Research Grants Council under Project CUHK14211823, and in part by the Chinese University of Hong Kong under Project 3134164 and Project 4055178. Recommended for acceptance by L. Duan. *(Xin Li, Yuxing Zhong, and Xinyuan Chuai are co-first authors.) (Corresponding authors: Xin Li; Junrui Liang; Wei-Hsin Liao.)*

Xin Li is with the School of Civil Engineering, Harbin Institute of Technology, Harbin 150001, China, also with the Department of Mechanical and Automation Engineering, The Chinese University of Hong Kong, Hong Kong SAR, China, and also with the Guangzhou Institute of Technology, Xidian University, Guangzhou 510555, China (e-mail: lixin.phd@gmail.com).

Yuxing Zhong, Xinyuan Chuai, Yaoyi Li, Weifeng Huang, Jiaming Chen, Xinming Zhang, Daxing Zhang, and Congsi Wang are with the Guangzhou Institute of Technology, Xidian University, Guangzhou 510555, China.

Guobiao Hu is with the Thrust of Internet of Things, The Hong Kong University of Science and Technology (Guangzhou), Guangzhou 511458, China.

Junrui Liang is with the School of Information Science and Technology, ShanghaiTech University, Shanghai 201210, China (e-mail: liangjr@shanghaitech.edu.cn).

Wei-Hsin Liao is with the Department of Mechanical and Automation Engineering, The Chinese University of Hong Kong, Hong Kong SAR, China (e-mail: whliao@cuhk.edu.hk).

This article has supplementary downloadable material available at https://doi.org/10.1109/TMC.2025.3640627, provided by the authors.

Digital Object Identifier 10.1109/TMC.2025.3640627

TABLE I
COMPARISON OF RELATED WORK: ENERGY HARVESTING AND INTERACTION PERFORMANCE

Year	Ref.	Transducer	Excitation	Energy Harvesting Performance			Interaction Evaluation		
				Power	Energy	Cold-start Latency	Input Tolerance[†]	Output Reliability[‡]	UI–Data Consistency[§]
2015	Chen et al. [14]	TENG	Keystroke tapping	69.6 μW/cm^2	N/A	N/A	N^a	N^c	N^d
2016	Li et al. [15]	TENG	Keystroke tapping	N/A	0.8mJ/1 hour typing at 6 Hz	N/A	N^a	N^c	N^d
2018	Wang et al. [16]	EM button + TENG	Keystroke tapping	$\sim$1.7 μW	$\sim$1.0 μJ/press	N/A	N^a	N^c	N^d
2021	Maharjan et al. [17]	EM button + TENG	Keystroke tapping	7.04 mW	N/A	N/A	N^a	N^c	N/A
2020	Fan et al. [18]	EM rotor	Arm motion	5.3 mW	N/A	N/A	N^a	N^c	N/A
2022	Teng et al. [19]	EM rotor	Arm motion	99 mW	N/A	$\sim$30 s	N^a	Y	N^d
2023	Arabi et al. [20]	EM rotor	Doors etc. handle actions	N/A	7–2900 mJ/action	N/A	N^a	N^c	N/A
2020	Pawełczak et al. [21]	EM button + PV	Light + Fingertip press	21.5 mW	0.66–1.98 mJ/press	N/A	N^a	Y	Y
2025	This Work	EM button	Fingertip press	1.64 W	7.2–8.8 mJ/press	$\sim$310 ms	Y	Y	Y

Abbreviations:
N/A = not available or not reported (no value or insufficient detail is provided for this metric); Y = criterion satisfied under the stated definition; N = criterion not satisfied or evidence insufficient to reach the stated threshold.
Header notes:
[†] Input Tolerance is judged strictly on excitation parameters (mechanical: force/velocity or displacement/frequency; optical: illuminance/angle; NFC/RF: distance/angle).
[‡] Output Reliability requires per-interaction output distributions or long-term stability bounds with acceptable variation.
[§] UI—Data Consistency requires transactional/confirmation semantics or end-to-end consistency under intermittency tests.
Row flags:
a = no excitation-parameter window reported; c = no per-interaction output distribution or stability bounds; d = no transactional/confirmation semantics.

hybrids [16], [17]. Yet the energy from a single press often cannot sustain a complete interactive loop, and the mismatch between peak power and load demand leads to output chattering and unstable peripherals. In practice, analog sensing with adequate bandwidth and signal to noise ratio in such keystroke tapping designs typically requires auxiliary power.

Beyond fingertip-only excitation, arm-motion harvesters can yield higher cumulative energy by aggregating larger mechanical excursions [18], [19], [20]. Rotor-based electromagnetic (EM-rotor) designs can deliver higher peak power but rely on large limb movements. They require sufficient swing amplitude and angular velocity to spin up the rotor and maintain flux variation. This design operates within a narrow excitation window across motion amplitude, velocity, and dwell time. Consequently, interaction outcomes are highly sensitive to excitation magnitude and variability. In Table I, interaction is assessed by input tolerance, output reliability, and user interface (UI) – data consistency. Here, input tolerance requires a reported excitation window with input ranges and interactive-loop success; output reliability per-interaction distributions or stability bounds with stated sample sizes; and UI–data consistency requires transactional or confirmation semantics across power interruptions. Under these criteria, most of the above designs show limited input tolerance, insufficient reporting of per-interaction output reliability, and a lack of guaranteed UI–data consistency under power interruptions.

Pawełczak et al. [21] developed a photovoltaic (PV)-powered Gameboy capable of interactive computing, with EM buttons assisting operation. It adopts an intermittent computing architecture that tracks memory usage and snapshots non-volatile storage to enable recovery after power interruptions. In terms of input tolerance, the effective window for user actions is narrow and sensitive to excitation magnitude and timing, and is further constrained by illumination variability and power buffering. Although intermittent runtimes and checkpointing improve recovery, frequent save and restore introduce nontrivial energy and latency overheads and do not ensure that every interaction clears the required energy threshold, especially under bursty or adversarial inputs [34], [35].

To address these challenges, we propose a kinetic energy harvester based on fingertip motion—the Fingertip Motion Harvester (FMH)—and a fully battery-free interactive gaming system, FMH-Game, powered exclusively by FMH units. As shown in Fig. 1, the proposed FMH incorporates an elastic-interconnected harvester coupled with a carefully engineered multistable structure, utilizing nonlinear dynamic behaviors and magnetic hysteresis to convert transient fingertip pressing motions into stable electrical pulses. By integrating an FMH

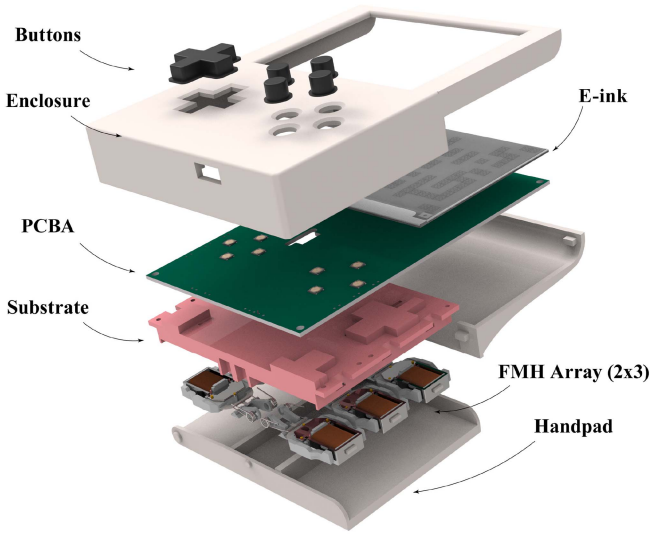

Fig. 1. The exploded view of the FMH-Game consists of an FMH array, a PCBA, an e-ink screen, control buttons, and enclosure structures.

array into the device enables atomic operations—saving the game state and updating the display—without introducing additional latency. We developed a full prototype and evaluated it via a gameplay task that calibrates energy from fingertip trigger to saved state and display update, supplemented by human-in-the-loop tests. Across repeated trials, per-actuation energy exceeded the task budget, demonstrating robust input tolerance, stable outputs, and UI– data consistency. As a result, even under intermittent energy and frequent power interruptions, FMH-Game remains responsive and robust, delivering a user experience comparable to that of battery-powered devices.

The contributions of this paper are summarized as follows:

1) We develop a fully battery-free interactive gaming architecture powered solely by fingertip kinetic energy, enabling continuous interactive gameplay without external power supplies.
2) We design a robust energy harvesting structure that ensures stable energy delivery, even under minimal and intermittent fingertip movements.
3) We implement an intuitive fingertip-based gaming solution that shows promise in promoting hand movements and enhancing fine motor skill exercises through engaging gameplay.

II. Overview

Fig. 1 shows an exploded view of the system, which includes a 2x3 FMH array, a printed circuit board assembly (PCBA), an e-ink display, control buttons, and enclosure structures. Fig. 2 presents an overview of kinetic-powered IoT systems featuring various energy buffering and release configurations. Mechanical energy generated from human motion is converted into electrical energy through electromechanical transducers, rectified and stabilized by a conditioning circuit, and subsequently used to power IoT tasks such as sensing, computation, and communication. Due to the inherent unpredictability and inconsistency of energy from human motion, the harvested energy often falls short of meeting the immediate and continuous power demands of IoT tasks. Therefore, managing energy buffers and their release is crucial for energy-driven IoT systems. Fig. 2(a) illustrates a common method that utilizes electrical energy buffering and release. In this method, capacitors store energy and then release it through an undervoltage lockout (UVLO) circuit, which helps regulate energy delivery.

The design of these system configurations is demand-oriented, ensuring that the energy and power requirements of IoT devices are met to complete a full sensing–computation–communication task. However, the complexity of these tasks is limited. More complex operations require excessive cold-start times for energy buffering, which can be a significant drawback. As a result, this method is typically restricted to discrete sampling tasks, such as measuring temperature or humidity.

Fig. 2(b) demonstrates a method used in intermittent computing for battery-free IoT devices, specifically involving a system with an electrical buffer and software-based energy release. In this approach, the designer employs intermittent computing to manage energy stored in the capacitor by dividing a complete task into multiple atomic subtasks. This segmentation reduces the energy buffering time and allows the system to track the progress of a task during power interruptions, enabling sequential execution of subsequent subtasks after a restart. This method facilitates the execution of more complex and lengthy application tasks. However, the instability of energy harvesting often leads to significant energy waste in checkpointing and state tracking. This inefficiency can leave insufficient energy to complete specific tasks, ultimately leading to poor real-time performance.

Fig. 2(c) shows the mechanical buffer and release method employed in the FMH. Mechanical buffers, which often use spring-based structures, store energy in response to external stimuli. In systems that receive intermittent or short bursts of energy input, this method ensures that enough energy is stored to meet or exceed the maximum energy requirements of all atomic operations, thereby enhancing the stability and reliability of the system. By further incorporating electrical energy buffering and release mechanisms, the system can execute complex interactive tasks more consistently. This integration allows for efficient management of intricate operations. Compared to existing solutions, the mechanical buffer and release method significantly improves system robustness, reduces task latency, and increases reliability, even in situations with irregular or intermittent energy inputs.

III. Fingertip Motion Harvesting

A. Modeling

Fig. 3(a) and (b) show the 3D model and schematic diagram of a single FMH, which comprises four primary components: (1) a moving body that contains a permanent magnet and a rotatable support rod equipped with magnetically conductive stoppers; (2) an iron core and coil assembly housed within a stationary outer case, which interacts magnetically with the moving body to generate electrical energy; (3) a cantilever buffer

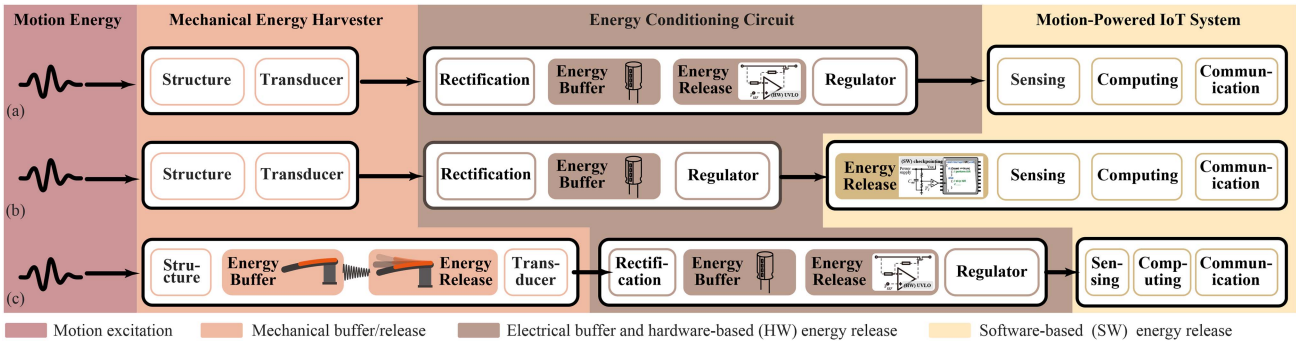

Fig. 2. Comparison of energy buffer and release configurations for kinetic-powered IoT system: (a) Electrical buffer and release with a capacitor and UVLO circuit for simple task; (b) Electrical buffer with software-based energy release for intermittent operation but with energy waste; (c) FMH-based mechanical buffer and release, offering higher robustness and reliability for irregular energy inputs.

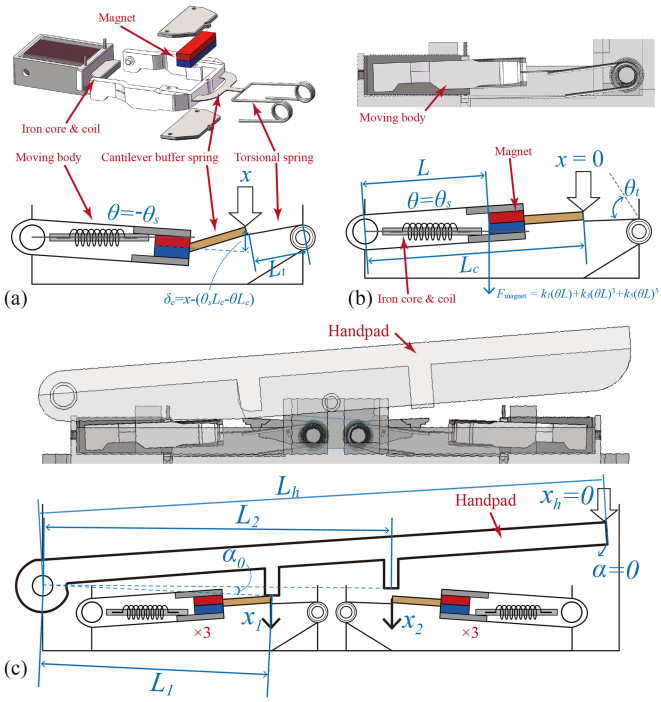

Fig. 3. The structure and schematic of the FMH. (a) and (b) Single FMH. (c) 2x3 FMH array.

spring that transmits and cushions the forces applied during fingertip pressing actions; and (4) a torsion spring (also known as the rebounding spring) that returns the moving body to its initial equilibrium position after each pressing motion.

Neglecting the impact of the torsion spring, the FMH is symmetric and mechanically bistable due to magnetic interactions. The moving body has two equilibrium points: one located above the dashed line and the other below it. The moving body rotates around the central axis on the left-hand side.

For each FMH, the total mechanical potential energy is given by:

$$U(x,\theta) = U_e(x,\theta) + U_m(\theta) + U_s(\theta). \tag{1}$$

Here, x is a prescribed external displacement imposed by the lever, and θ is the internal rotational coordinate solved from equilibrium or dynamics; hence x and θ are not independent. In quasi-static analysis, $\theta(x)$ follows from the equilibrium condition $\partial U/\partial\theta = 0$, where the magnetic torque from $U_m(\theta)$, i.e., $\frac{\partial U_m}{\partial\theta} = [k_1(\theta L) + k_3(\theta L)^3 + k_5(\theta L)^5], L^2$, enters the balance and thereby influences the external force in (6). The term U_e represents the elastic potential energy derived from the cantilever buffer spring and the torsion spring. It is a function of the finger position x and the angular position θ of the moving body. U_m denotes the magnetic potential energy between the magnet and the iron core, and it is a function of θ. Lastly, U_s represents the potential energy contribution from the contact interactions between the moving body and the stoppers, which impose mechanical constraints and modify the system's energy landscape by introducing nonlinear boundary effects. The elastic potential energy can be expressed as:

$$U_e(x,\theta) = \frac{1}{2}k_c(x + \theta L_c - \theta_s L_c)^2 + k_t\left(\frac{1}{2}\frac{x^2}{L_t} + \theta_t x\right) \tag{2}$$

where k_c is the stiffness coefficient of the cantilever buffer spring, L_c is the distance from the end of the cantilever buffer spring to the center axis on the left-hand side, and θ_s is the critical angular displacement when the moving body touches the stopper. Similarly, k_t, L_t, and θ_t denote the stiffness, effective lever arm length, and pre-tightening angle of the torsion spring, respectively. The cantilever buffer spring force is defined as:

$$F_c = k_c\delta_c \tag{3}$$

where δ_c is the vertical displacement difference between the cantilever spring's two ends, as illustrated in Fig. 3(a).

The magnetic potential energy $U_m(\theta)$ is modeled using a nonlinear Duffing-type polynomial approximation:

$$U_m(\theta) = \frac{1}{2}k_1(\theta L)^2 + \frac{1}{4}k_3(\theta L)^4 + \frac{1}{6}k_5(\theta L)^6 \tag{4}$$

where k_1, k_3, and k_5 are fitted magnetic potential coefficients, and L is the equivalent lever arm associated with the magnet–core interaction. The coefficients play distinct roles: k_1 sets the near-equilibrium curvature (effective stiffness) of U_m with respect to the generalized displacement (θL); k_3 provides the leading nonlinear correction that, together with k_1, shapes the well depths and barrier height; and k_5 captures higher-order hardening and regularizes the potential at larger amplitudes. The fitted values and units (referenced to the polynomial variable

TABLE II
PARAMETERS OF THE PROTOTYPED FMH AND FMH ARRAY

Parameter	Description	Value
k_1	Magnetic potential coefficient (quadratic term)	-1.10e3 $\mathrm{N\,m^{-1}}$
k_3	Magnetic potential coefficient (quartic term)	-11.53e9 $\mathrm{N\,m^{-3}}$
k_5	Magnetic potential coefficient (sextic term)	6.99e15 $\mathrm{N\,m^{-5}}$
k_s	Stopper equivalent stiffness	1.00e9 $\mathrm{N\,m^{-1}}$
θ_s	Maximum angle of moving body	2.47 °
θ_t	Torsion spring preload angle	33.52 °
L_t	Torsion spring lever	14.38 mm
L	Magnetic equivalent lever	22.01 mm
L_c	Cantilever spring lever	26.45 mm
k_c	Cantilever spring stiffness	3.12e3 $\mathrm{N\,m^{-1}}$
k_t	Torsion spring stiffness	9.75 $\mathrm{N\,rad^{-1}}$
α_0	Handpad terminal lever angle difference	1.28 °
L_1	Handpad inner terminal lever	34.28 mm
L_2	Handpad outer terminal lever	63.81 mm
L_h	Handpad lever	105 mm

Note: Units of k_1, k_3, and k_5 are referenced to the polynomial variable (θL) in $U_m(\theta)$ (θ dimensionless, L in meters). Coefficients were identified by least-squares fitting to quasi-static magnet–core measurements, detailed procedures and data are provided in the supplementary Figs. S2–S4.

(θL)) are summarized in Table II. The potential energy contribution from the stoppers can be simply described as:

$$U_s(\theta) = \frac{1}{2}k_s(\theta L - \theta_s L)^2 \langle \theta L - \theta_s L > 0 \rangle + \frac{1}{2}k_s(\theta L + \theta_s L)^2 \langle \theta L + \theta_s L < 0 \rangle \quad (5)$$

where k_s is the equivalent stiffness representing the limiting effect of the stopper, and $\langle \bullet \rangle$ is the Heaviside unit step function. The force applied by the finger at any moment is a combination of the cantilever buffer spring and the torsion spring, formulated as

$$F = k_t\left(\frac{x}{L_t} + \theta_t\right) - k_c(-\theta L_c + \theta_s L_c - x) \quad (6)$$

The FMH array is arranged in a 2×3 configuration, as depicted in Fig. 3(c). They are simultaneously triggered by a lever-structured handpad. The handpad transmits fingertip forces, inducing displacements at multiple actuation points of the FMHs.

Assuming that the external displacement applied by the hand at the handpad actuation point is x_h, the total potential energy stored in the three FMHs near the handpad rotation axis (left-side FMHs) can be calculated as:

$$U_1(x_h, \theta) = 3U(x_1, \theta) \quad (7)$$

where the displacement x_1 at the left-side FMHs' actuation points is related to the external displacement x_h by the lever structure as:

$$x_1 = x_h \frac{L_1}{L_h} \quad (8)$$

where L_h is the lever arm length from the external force application point (hand position) to the handpad pivot, and L_1 is the lever arm distance from the pivot to the actuation points of the left-side FMHs.

Similarly, for the three FMHs located farther from the handpad rotation axis (right-side FMHs), the total potential energy is expressed as:

$$U_2(x_h, \theta) = 3U(x_2, \theta) \quad (9)$$

where the displacement x_2 at the actuation points of the right-side FMHs is given by:

$$x_2 = \left(\frac{x_h}{L_h} - \alpha_0\right) L_2 \langle x_h > \alpha_0 L_h \rangle \quad (10)$$

where L_2 is the lever arm length from the pivot to the actuation points of the right-side FMHs, and α_0 is the angular offset between the lever arms L_1 and L_2.

The total external force exerted at the handpad actuation point (hand position) is the sum of forces from all six FMHs transmitted through the lever mechanism:

$$F_h = 3\frac{F_1 L_1}{L_h} + 3\frac{F_2 L_2}{L_h} \langle x_h > \alpha_0 L_h \rangle \quad (11)$$

where F_1 and F_2 denote the forces at the actuation points of the left-side and right-side FMHs, respectively. These forces are derived by substituting the corresponding displacements x_1, x_2, and angular positions θ into equation (6).

B. Mechanical Energy Buffer and Release

A single fingertip motion cycle for the FMH comprises three distinct phases: (1) mechanical potential energy storage, (2) instantaneous release of mechanical potential energy, and (3) return to the initial stable position. Fig. 4(a) and (b) illustrate the complete cycle, along with corresponding potential energy distribution at different FMH positions, demonstrating how fingertip motion energy is captured and converted into electrical energy via mechanical switching. The parameters of the prototyped FMH are shown in Table II.

At the initial position P1 (with displacement $x = 0$), the FMH remains stably positioned at the bottom of the left-side potential well in the absence of external force. As the fingertip presses downward onto the cantilever buffer spring (positions P1–P5), the spring undergoes elastic deflection, gradually accumulating mechanical potential energy. This energy storage process is visually represented by the increasing height along potential well-1 (see red arrow marked "1" in Fig. 4(b)). As the fingertip continues pressing downward and reaches the critical position P5, the mechanical potential energy stored in the cantilever buffer spring reaches its maximum threshold. At this critical position, the accumulated elastic restoring force overcomes the magnetic attraction that maintains the moving body in the toggled-up state, triggering a rapid transition to the toggled-down state (position P5'). During this transition, the potential barrier separating the bistable potential wells disappears, allowing the FMH to spontaneously shift toward potential well-2, as indicated by the red arrow in inset P5' of Fig. 4(a). This spontaneous transition instantaneously releases mechanical potential energy, initiating

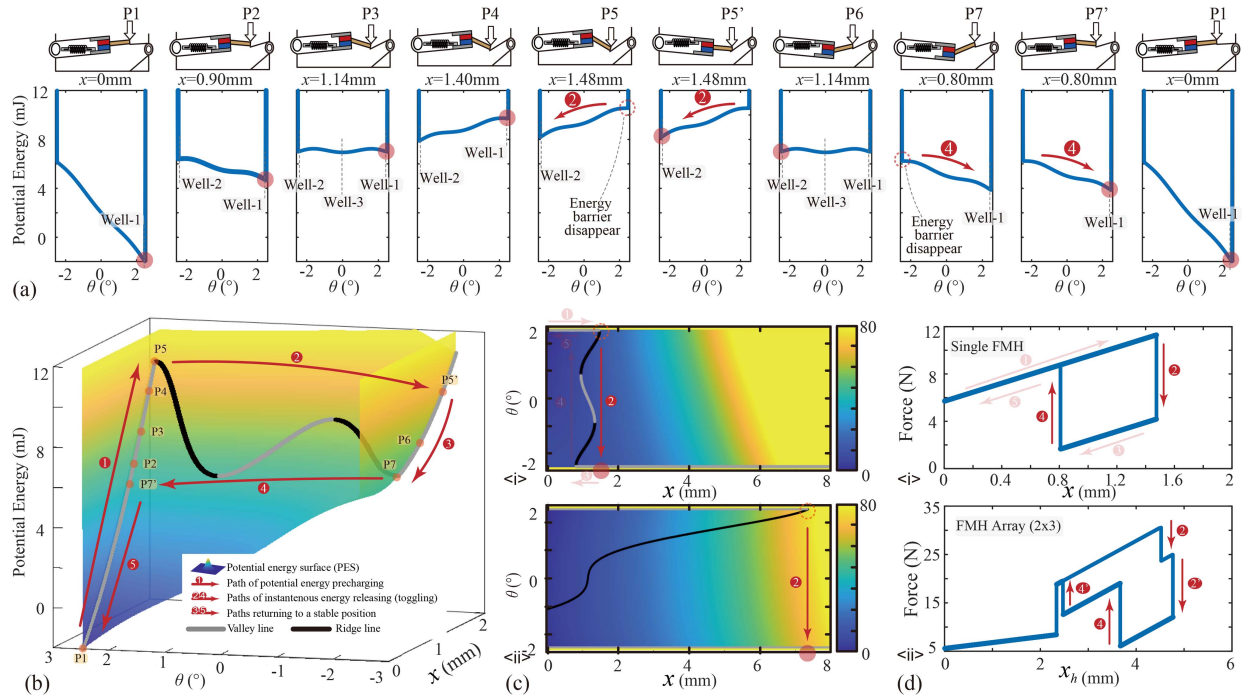

Fig. 4. Dynamic and operation mechanism of the FMH. (a) Different states of the FMH throughout one toggling cycle and corresponding potential energy profiles during the fingertip cycle. (b) 3D potential energy evolution during the fingertip cycle. Solid black lines represent valleys (stable equilibrium positions), dashed curves represent ridges (potential barriers), and red arrows indicate the process proceeding direction. (c) 2D contour plots of potential energy: <i>Demonstration of the transient third potential well (well-3) with a cantilever spring stiffness of 3.12×10^3 N m^{-1}; <ii>Parametric analysis shows suppression of well-3 with reduced cantilever spring stiffness, where the cantilever spring stiffness coefficient is reduced to $0.2\times$ its original value. (d) Force-displacement loops during energy harvesting: <i>Single FMH cycle showing two energy release events; <ii>amplified force-displacement behavior observed in the 2×3 FMH array.

the first energy conversion. The magnitude of the released energy corresponds to the vertical coordinate difference between positions P5 and P5' (see red arrow marked "2" in Fig. 4(b)).

Upon releasing fingertip pressure (positions P6–P7), the cantilever buffer spring deflects upwards, generating a restoring force on the moving body. Initially, magnetic attraction holds the system in the toggled-down state, with the iron core in contact with the upper stopper. Once the fingertip retracts beyond a critical displacement, the combined upward restoring forces from the buffer and torsion springs surpass the magnetic attraction. Consequently, the moving body rapidly returns to the toggled-up state (transition from P7 to P7'), releasing stored potential energy for a second time and resetting the system for the next cycle of electromechanical energy conversion. Similar to the previous transition, this second spontaneous release is marked by the disappearance of the potential barrier between the two potential wells (see red arrow marked "4" in Fig. 4(b)).

Fig. 4(b) provides a more detailed three-dimensional visualization of the dynamic potential energy transitions during a single fingertip motion cycle. The coarse gray solid line represents the valley path (stable equilibrium positions), while the coarse black solid line represents the ridge (potential barrier), which acts as the potential barrier separating the two wells. Initially, at initial position P1, the system remains stably at the bottom of the left-side valley. As the fingertip presses down, the potential energy gradually increases along the left-side valley path. At the critical point P5, the ridge converges with the valley, eliminating the barrier and triggering a spontaneous "sliding" transition to the lower right-side valley path (position P5'). During this rapid transition, mechanical potential energy equivalent to the height difference between P5 and P5' is released. As the fingertip retracts, the system moves upward along the right-side valley path until reaching the second critical position P7, where the barrier disappears once again. This leads to a second spontaneous transition back to the initial valley path and completing the cycle at position P1.

At both critical toggling positions (P5→P5' and P7→P7'), the moving body undergoes a rapid snap-through that flips the magnetic polarity across the core. This produces a large flux-change rate and steep induced waveforms concentrated within a short time window. Each event yields sharp voltage and current pulses whose amplitudes reflect the released mechanical potential and the coil coupling. These pulses are efficiently rectified, delivering high instantaneous power.

In summary, each single fingertip press-and-release motion induces two rapid spontaneous transitions of the FMH moving body, each accompanied by an instantaneous release of mechanical potential energy. The amounts of energy released during these transitions are quantitatively represented by the vertical coordinate differences between points P5–P5' and P7–P7' in Fig. 4(b).

C. Three-Potential-Well Phenomenon

The FMH generally has two stable equilibrium states, where the core is in contact with either the upper or lower magnetically conductive stopper. However, under certain intermediate conditions, a third potential well (well-3) can transiently emerge. As

illustrated in Fig. 4(a) and (b), the intermediate positions P3 and P6 correspond to this temporary equilibrium state. This is visually depicted as an additional valley path (gray solid line) in the three-dimensional potential energy plot (Fig. 4(c)).

The formation of well-3 arises when two conditions are satisfied: (1) the magnetic attraction forces between the core and stoppers approach equilibrium at approximately zero angular deflection ($\theta \approx 0$), and (2) the cantilever buffer spring aligns horizontally, becoming essentially force-neutral. Under these circumstances, residual spring forces exactly counterbalance the weak magnetic interactions, creating a metastable equilibrium. However, due to the absence of sustained external forces, this intermediate equilibrium is inherently unstable and only exists transiently.

Parametric analysis results in Fig. 4(c)<i> and <ii> show that reducing the cantilever spring stiffness coefficient to 0.2 times its nominal value effectively suppresses the formation of well-3. This adjustment significantly enhances the mechanical energy released during each switching event, increasing it by 273.9% . However, it also comes with notable trade-offs, including a 35.2% rise in the triggering force, which could compromise user comfort, and a 398.9% increase in actuation displacement, necessitating a much larger fingertip motion. Therefore, optimizing FMH performance requires careful consideration of these trade-offs between energy efficiency and usability for human-machine interface applications.

In practical operation, the transient state, i.e., well-3, remains inaccessible, as the system spontaneously transitions back to one of the conventional bistable equilibrium states (positions P2 or P4) during continued fingertip pressing or release. This pseudo-tristable behavior is purely transitional and does not compromise the operational reliability or energy harvesting efficiency of the FMH.

D. Array Configuration for Enhancement

The FMH's force–displacement characteristics play a critical role in determining the mechanical energy input, the corresponding electromechanical conversion performance, and user experience. Fig. 4(d) presents the experimental and simulation results that illustrate the mechanical response during a full actuation cycle.

As shown in Fig. 4(d)<i>, a single FMH unit exhibits a distinct hysteresis loop during the pressing–releasing cycle. This loop contains two sharp transitions, corresponding to the toggling events of the bistable structure—first during the downward press and then during the upward release. Each transition represents an instantaneous energy release event, contributing to the overall electromechanical conversion. The enclosed area within the loop quantifies the mechanical energy input per cycle, validating the bistable dynamics and energy capture mechanism of the FMH.

To enhance the energy harvesting performance and increase the total energy output per interaction, multiple FMH units can be integrated into an array configuration. When scaled to a 2×3 array configuration, the aggregated mechanical response (Fig. 4(d)<ii>) demonstrates significantly amplified force–displacement behavior. The array maintains the characteristic hysteretic profile while achieving higher total input energy, confirming that the individual FMH units are effectively coordinated. Notably, although the array configuration enhances the overall harvested energy, a well-designed mechanical coupling mechanism is essential to ensure consistent triggering of energy release events across all units. To achieve this, the FMH-Game incorporates a specialized handpad design, as detailed in one of the following sections.

These experimental results affirm the reliability and scalability of the FMH design. The consistent force–displacement behavior across individual and array configurations ensures predictable energy input, which is essential for delivering a stable and robust energy source for battery-free interactive systems.

IV. FMH-Game

A. Hardware Design

As shown in Fig. 5, the FMH-Game hardware consists of four main modules: 1) rectification unit, 2) electrical energy buffer and release unit, 3) regulator unit, and 4) gaming interaction unit.

1) *Rectification Unit:* AC pulses from the FMH array are converted to DC using a full-wave bridge built with SS34 Schottky diodes to reduce conduction loss and support transient peaks.

2) *Electrical Energy Buffer and Release Unit:* Intermittent harvested energy is buffered by a storage capacitor C_{sto}. A UVLO circuit regulates energy release via capacitor-voltage thresholds, enabling output only within the designated window and ensuring sufficient buffered energy for each interaction. This mechanism prevents undervoltage, protects downstream electronics, and stabilizes energy availability for subsequent modules.

3) *Regulator Unit:* After release, energy is conditioned to a single logic rail to decouple game timing from harvester variability. A 3.3 V rail is provided by the LTC3588 energy-harvesting power management IC configured as a low-quiescent buck regulator, ensuring stable operation during short, high-demand display or memory transactions.

4) *Gaming Interaction Unit:* A low-power microcontroller (MCU, nRF52832) manages user input and display sequencing. This unit also integrates non-volatile random-access memory (NVRAM), user interface buttons, and a non-volatile e-ink display. In this design, the use of Ferroelectric Random Access Memory (FRAM, MB85RS256BPNF)-based NVRAM ensures reliable and persistent data storage, preserving game states and user progress even during power interruptions. Additionally, the e-ink display can maintain visual content without requiring continuous power, which significantly enhances energy efficiency.

B. Game Interaction Design

Ensuring reliable operation and a seamless user experience in battery-free interactive gaming systems is challenging under unstable energy conditions and has been studied in intermittent and battery-free systems, including checkpointing, transactional execution, and the use of non-volatile displays. To illustrate the

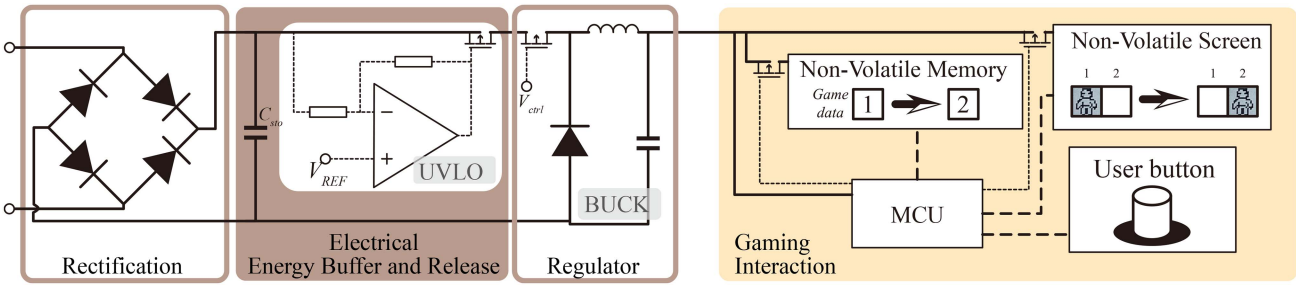

Fig. 5. Hardware design of the FMH-Game. The fingertip harvester output is fullwave rectified and accumulated on a storage capacitor. An energy buffer-and-release circuit with UVLO/threshold detection gates the stored energy to the load. A buck regulator provides a stable supply for the digital and display modules. The gaming interaction block integrates MCU, non-volatile memory, e-ink display, and user buttons, enabling checkpointing and power-failure-safe updates.

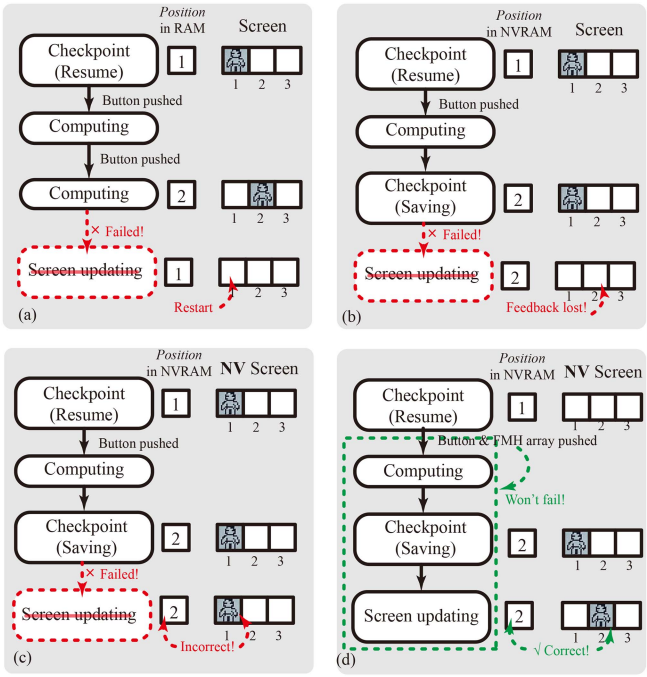

Fig. 6. Game interaction design of the FMH-Game: (a) Volatile RAM with Volatile Screen loses all data and visuals during power interruptions; (b) NVRAM with Volatile Screen retains data but loses visual states; (c) NVRAM with NV Screen retains data and visuals but risks mismatches; (d) FMH with NVRAM and NV Screen ensures synchronized data and visuals with consistent energy harvesting.

challenge and our solution, we compare four typical strategies for managing atomic operation, as shown in Fig. 6.

a) *Volatile RAM with Volatile Screen:* Conventional designs utilize volatile RAM and volatile screens (e.g., LCDs) for rapid response. However, these components lose all stored data and visual content upon a power interruption, so the system must restart from the last stable checkpoint, forcing users to repeat their actions and impairing the interaction quality.

b) *NVRAM with Volatile Screen:* Using NVRAM (e.g., FRAM) for checkpointing improves data persistence and helps minimize data loss upon interruptions. However, the volatile screen still loses visual states during power outages. When the system restarts, the restored checkpoints may not match the blank or default visual states, leading to user confusion and a disruption in gameplay continuity.

c) *NVRAM with NV Screen:* Integrating NVRAM checkpointing with the NV screen further enhances data persistence. Nevertheless, interruptions during the short period between checkpoint storage and display updating can still lead to mismatches. For example, if the stored checkpoint state (e.g., position 2) differs from the partially updated visual content (e.g., position 1), the discrepancy may mislead users and degrade the interaction quality.

d) *FMH with NVRAM and NV Screen:* To effectively address these limitations, FMH-Game integrates precisely timed NVRAM checkpointing with an e-ink screen. Each user interaction initiates a strictly controlled sequence: first, the current game state is saved in NVRAM, followed immediately by an update to the e-ink display. The e-ink display preserves visuals during unexpected power interruptions, allowing synchronization between the stored checkpoints and the displayed content. Furthermore, to enhance reliability and responsiveness, FMH-Game utilizes an FMH array that is precisely calibrated to meet the energy demands of atomic tasks. Each user activation reliably generates at least 7.2 mJ, which is sufficient to complete checkpointing and display updating operations without interruption or latency. This exact energy matching guarantees a consistent interaction quality, providing a smooth and responsive gaming experience comparable to traditional battery-powered platforms.

C. Software Design

Fig. 7 presents the software state machine diagram, highlighting the MCU control logic, peripheral interactions, and energy management strategy. During initial system startup (cold-start), the user actuates the FMH array twice, charging the storage capacitor voltage (V_{sto}) above the UVLO threshold. Once the threshold is reached, the MCU powers on and initializes essential peripherals, including the FRAM. Immediately thereafter, the MCU retrieves previously saved game state and pixel data from FRAM through SPI communication, ensuring a seamless gameplay experience. To minimize idle energy consumption, the MCU directly manages FRAM power, enabling it only during brief read/write operations.

After initialization and data retrieval, the MCU processes user inputs from the interface buttons, computes updated game states and their corresponding visual images, and promptly stores the newly computed checkpoint data (game progress and

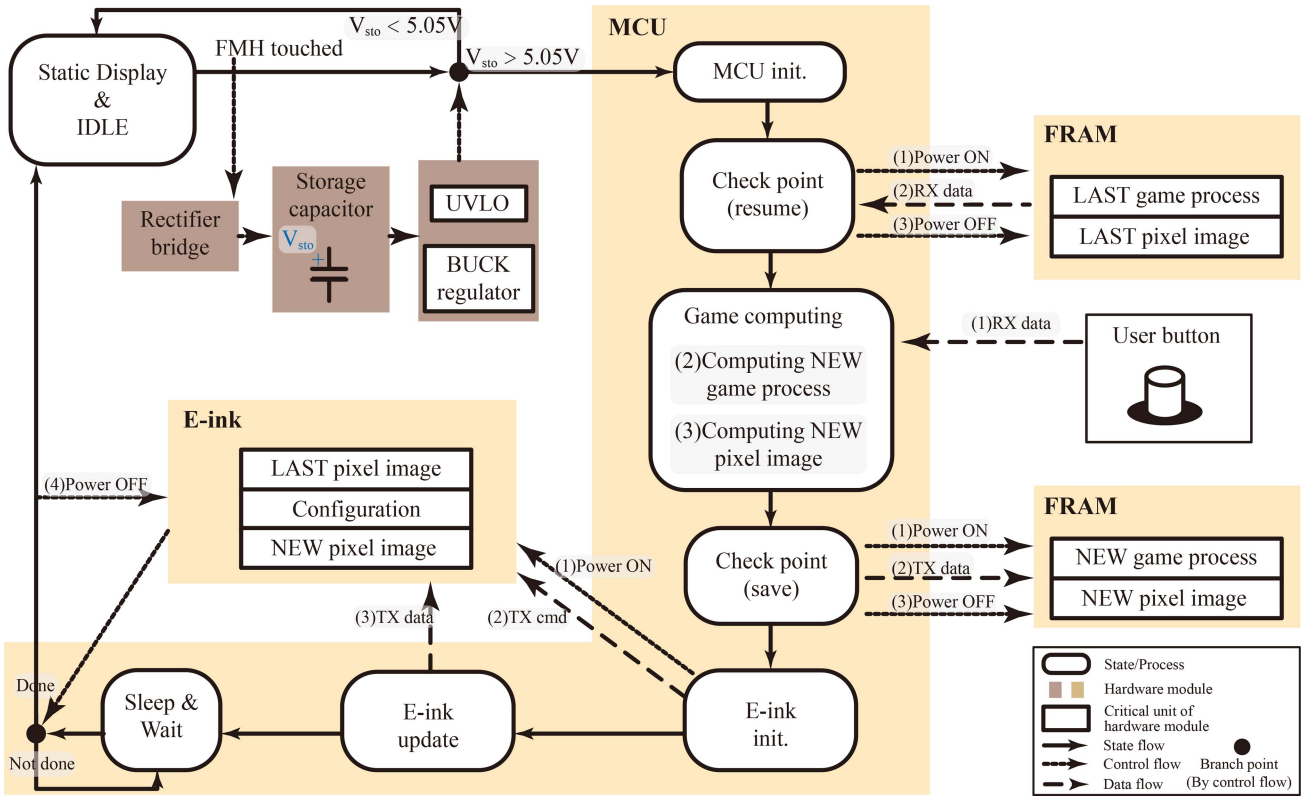

Fig. 7. Software state machine design of the FMH-Game. The MCU state machine manages initialization, checkpointing, and e-ink updates, ensuring reliable operation and seamless gameplay continuity with precise energy matching.

pixel images) back into FRAM. By utilizing the non-volatile characteristics of FRAM, we can ensure reliable preservation of game state data, even during potential power interruptions.

After the updated data is checkpointed, the MCU activates and initializes the e-ink display, transmitting configuration commands and updated image data through SPI. This synchronization effectively prevents visual and data inconsistencies, significantly enhancing user experience.

During the refresh cycle of the e-ink display, which typically lasts several hundred milliseconds, the MCU enters a low-power sleep mode, awaiting an interrupt from the display module signaling refresh completion. This interrupt-driven sleep mechanism significantly reduces energy consumption, enhancing the overall energy efficiency of the system. Upon receiving this interrupt, the MCU immediately powers down the display and returns to an ultra-low-power idle state, awaiting subsequent user interactions.

For subsequent interactions occurring within short intervals, typically a single actuation of the FMH array suffices to recharge the capacitor voltage above the UVLO threshold. The energy harvested from the FMH is tailored to match the energy demands of atomic tasks, including MCU initialization, FRAM checkpointing, and e-ink display updating. This precise energy budgeting minimizes latency and ensures consistently responsive interactions, comparable to traditional battery-powered gaming systems.

By integrating optimized peripheral control, non-volatile data checkpointing, interrupt-driven low-power management, and precise energy matching, the software design guarantees reliable operation, seamless gameplay continuity, and an exceptional user experience, effectively addressing the challenges posed by unstable energy availability.

V. Evaluation

A. Implementation

To validate the proposed concept, a fully functional prototype of the FMH-Game was developed, as shown in Fig. 8. The system integrates multiple key components into a compact and ergonomic plastic enclosure, optimized for user interaction and energy harvesting. The front view (Fig. 8(a)) highlights the 4.2-inch e-ink display and physical control buttons, which serve as the main user interface. The actuation mechanism of the FMH array operates through a two-step fingertip interaction process (Figs. 8(b)–(c)). During each gameplay interaction, the user first presses one of the directional buttons to indicate a move (Step #1), followed by pressing the central handpad (Step #2). This second step activates the 2×3 FMH array embedded beneath the handpad, generating sufficient energy to perform the full sequence of computing and display tasks required for one atomic operation.

Fig. 8(d) provides an exploded view of the device assembly, showcasing the integration of all critical modules: (1) the front enclosure panel, which ensures durability and ease of use; (2) the PCBA that contains the rectification circuit, electrical energy buffer ($C_{\text{sto}} = 1000\,\mu\text{F}$) and release circuitry (UVLO,

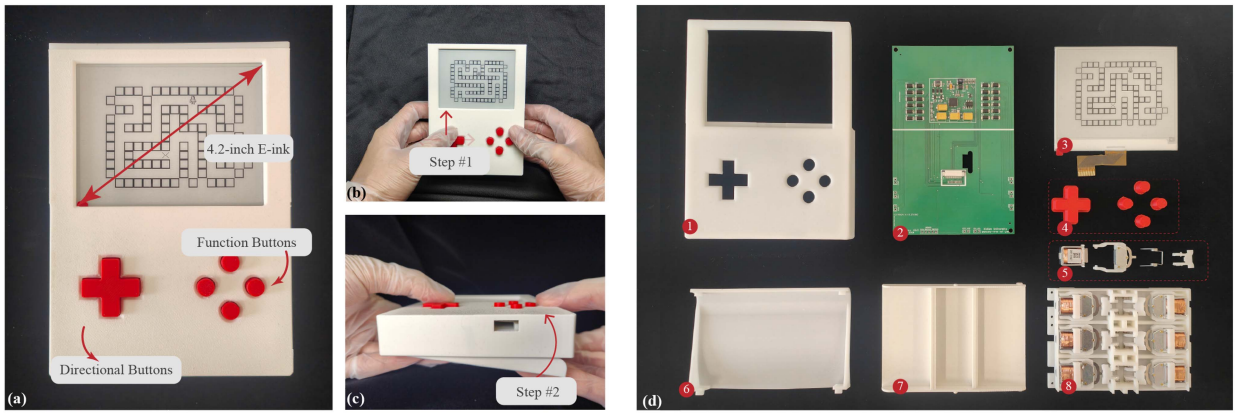

Fig. 8. Prototype implementation of the FMH-Game. (a) Front view, highlighting the 4.2-inch e-ink screen and user interface buttons. (b)-(c) Typical two-step fingertip actuation process: pressing the directional buttons (Step #1), followed by the handpad (Step #2) to generate sufficient energy for gameplay interactions. (d) Exploded view of the prototype components: (1) Front enclosure panel; (2) PCBA with rectification, energy buffer and release, regulator, computing, and display circuits; (3) 4.2-inch e-ink screen; (4) Buttons; (5) Assembly of a single FMH; (6) Back enclosure cover; (7) Handpad; and (8) FMH array integrated with the substrate.

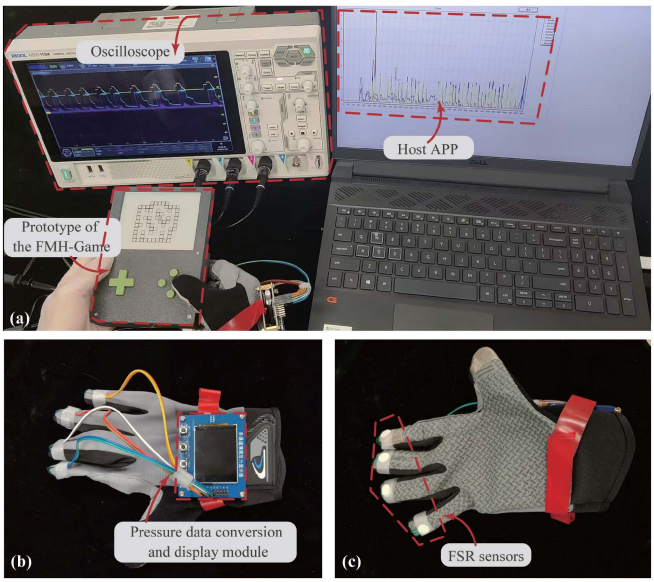

Fig. 9. Experimental setup for synchronized electrical and force measurements during gameplay. (a) Oscilloscope traces: regulator supply voltage, storage-capacitor voltage, and load current of the gaming interaction unit; force waveform recorded concurrently via a pressure glove and a laptop host app. (b) Pressure-glove apparatus with on-glove conversion/display. (c) Placement of FSR sensors at the fingertips of the index, middle, ring, and little fingers to capture handpad forces.

configured in the range between 3.67 V and 5.05 V), voltage regulation, MCU-based computing, and display control; (3) the 4.2-inch e-ink display; (4) tactile user input buttons; (5) an individual FMH unit; (6) the rear enclosure cover; (7) the handpad for mechanical actuation; and (8) the 2×3 FMH array integrated onto a structural substrate.

B. Measurement Setup and Evaluation Criteria

To characterize the electrical and mechanical behaviors during gameplay, we built a synchronized measurement setup, as shown in Fig. 9. Electrical signals were captured with a digital oscilloscope through dedicated channels for: (1) the charging voltage of the storage capacitor; (2) the regulator supply voltage; and (3) the load current drawn by the gaming interaction unit, which includes the MCU and peripherals. In parallel, fingertip forces applied to the handpad were recorded using a pressure glove instrumented with force-sensitive resistors (FSR) sensors on the index, middle, ring, and little fingers; a host application logged the force waveforms and provided timestamps for alignment with the oscilloscope traces. In addition, the standalone force-characterization setup is shown in Fig. S1 and the energy-harvesting repeatability setup is shown in Fig. S5 in the Supplementary Materials.

For each test, participants executed the two-step interaction (directional key followed by handpad), while all channels were recorded with synchronized timestamps. The metrics in Table I are obtained as follows: (1) Power is computed from the rectified harvester voltage/current and reported as the average deliverable power at the regulator input; (2) Energy per press is derived from the net change of the storage capacitor; (3) Cold-start latency is defined as the interval from the initial actuation to the onset of regulated output; (4) Input tolerance is determined by sweeping handpad force profiles and identifying the range that completes one atomic operation through the complete interaction loop; (5) Output reliability is assessed from per-press distributions of delivered energy and load-current envelopes, requiring bounded variation during computation and e-ink refresh; and (6) UI–data consistency is verified by firmware transactional commits cross-checked against host-app logs and oscilloscope timestamps to ensure a one-to-one mapping between interactions and state updates.

C. Energy Harvesting Performance

The dynamics of the proposed FMH and FMH array are rigorously designed to optimize the conversion of mechanical energy from fingertip pressing–releasing actions into electrical energy. Fig. 10 presents the experimental results, offering detailed insights into the energy harvesting process.

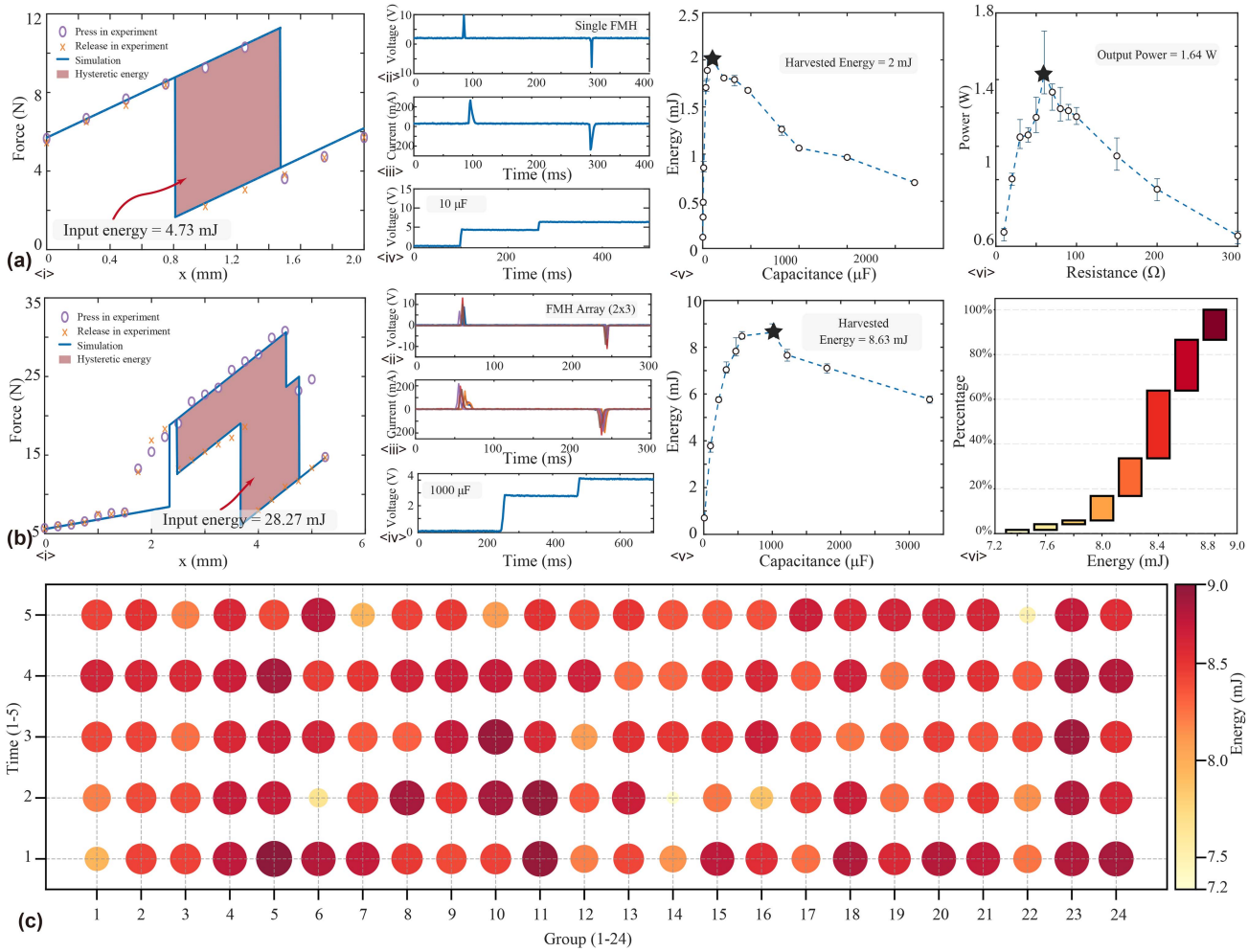

Fig. 10. Performance evaluation of FMH dynamics and energy harvesting. (a) Performance of a single FMH unit: <i>Force–displacement relationship showing mechanical energy input during one pressing–releasing cycle, validated by experimental measurements and simulations; <ii>Transient open-circuit voltage response; <iii>Transient short-circuit current response; <iv>Voltage dynamics of the capacitor during a single pressing–releasing cycle; <v>Capacitor charging test revealing a harvested energy of 2 mJ; <vi>Output power versus load resistance showing a peak power of 1.64 W. (b) Performance of a 2×3 FMH array: <i>Force–displacement relationship and mechanical energy input, demonstrating scalability of the mechanical design; <ii>Transient open-circuit voltage response; <iii>Transient short-circuit current response; <iv>Voltage dynamics of the capacitor during a single pressing–releasing cycle; <v>Capacitor charging test revealing a harvested energy of 8.63 mJ; <vi>Histogram of harvested energy distribution from repeated tests, demonstrating consistent energy outputs ranging from 7.2 mJ to 8.8 mJ. (c) Heatmap of harvested energy distribution across 24 groups, demonstrating robustness and consistency of the FMH array in practical usage scenarios.

Fig. 10(a)<i> illustrates the force–displacement relationship of a single FMH unit, showing a strong agreement between experimental measurements and simulations. The enclosed hysteresis loop represents the mechanical energy input during one pressing–releasing cycle, quantified as 4.73 mJ. This validates the developed model in predicting energy transfer dynamics. The transient open-circuit voltage (Fig. 10(a)<ii>) and short-circuit current (Fig. 10(a)<iii>) responses exhibit sharp pulses, indicative of instantaneous electromechanical energy conversion during the deformation and release phases. Under optimal impedance-matching conditions, the capacitor charging curves (Fig. 10(a)<iv> and <v>) indicate a harvested energy of approximately 2.00 mJ per actuation, computed from the net increase of capacitor energy during a single pressing–releasing event. Furthermore, under the resistance sweep that maximizes output power, the peak value reaches 1.64 W, as shown in Fig. 10(a)<vi>. This peak is consistent with snap-through events during each press–release, where rapid polarity flips produce large flux-change rates and sharp voltage/current pulses that are efficiently rectified. With the alternating-polarity FMH, the resulting single-unit power and power density exceed those of comparable harvesters reported in Table I.

The integration of multiple FMH units into a 2×3 array results in a substantial improvement in energy harvesting performance, as shown in Fig. 10(b). The force–displacement curve (Fig. 10(b)<i>) again closely aligns with simulation results, confirming the scalability of the mechanical model to an array configuration. The corresponding hysteresis loop indicates an input mechanical energy of 28.27 mJ, significantly greater than that of a single FMH unit. The transient voltage (Fig. 10(b)<ii>) and current (Fig. 10(b)<iii>) responses reveal that individual FMH units within the array are activated

sequentially, attributed to slight manufacturing tolerances. Capacitor charging tests conducted under optimal impedance-matching conditions (Fig. 10(b)<v>) show that the peak harvested energy reaches 8.63 mJ per actuation. Repeated measurements yield consistent outputs ranging from 7.2 mJ to 8.8 mJ, with most values concentrated between 8.4 mJ and 8.8 mJ, as shown in Fig. 10(b)<vi> and Fig. 10(c). While overall efficiency is informative, human-motion energy harvesters are primarily assessed by practically deliverable energy per actuation, power at matched load, and capacitor-charging behavior under realistic use, which directly determine task sufficiency.

To examine the robustness and consistency of the FMH array, extensive repeated tests were conducted across 24×5 groups, with each group performing five consecutive fingertip actuations. Fig. 10(c) presents the harvested energy distribution as a heat map. It reveals that the harvested energy consistently exceeds the minimum energy budget of 5.75 mJ required for a single game interaction. These results confirm the reliable energy harvesting capability of the FMH array under practical usage conditions.

D. Per-Actuation Conversion Efficiency

For per-actuation conversion efficiency, we report the ratio is obtained from the area of the measured force–displacement hysteresis loop of the mechanical buffer, and $E_{\text{harvested}}$ is the single-actuation increase of capacitor energy under impedance matching. For a single FMH, $\eta \approx 42\%$ with $E_{\text{input}} = 4.73\,\text{mJ}$ and $E_{\text{harvested}} \approx 2.00\,\text{mJ}$; for the 2×3 array, $\eta \approx 30.5\%$ with $E_{\text{input}} = 28.27\,\text{mJ}$ and $E_{\text{harvested}} = 7.2$–$8.8\,\text{mJ}$.

However, an overall efficiency alone is insufficient to characterize human-motion harvesters: the input is user-dependent and nonstationary (force amplitude, stroke, velocity, dwell, timing), precluding a unique denominator; and system-level elements intentionally trade energy for stability and compatibility, so a single scalar obscures usable energy delivered to storage. Accordingly, we report a reproducible per-actuation conversion ratio and adopt application-facing metrics—harvested energy per actuation and precise energy budgeting aligned to the software execution flow—which directly determine tasklevel sufficiency and are supported by the measurements below.

To ensure stable operation under intermittent energy supply, the FMH-Game adopts precise energy budgeting aligned with its software execution flow (Fig. 7). Each user interaction is executed atomically within a single energy cycle—from capacitor charging and system wakeup to computation and visual output—whose peroperation energy and latency are summarized in Table III. When the buffer exceeds threshold, the system starts the MCU, resumes from the last checkpoint, computes the game state (single-step or next-level), and checkpoints to FRAM, followed by e-ink operations. The e-ink display consumes energy only during refresh (initialization, data transfer, and local/global refresh); the MCU sleeps during refresh and resumes on interrupt. Overall, a single-step interaction costs about 5.75 mJ in 908 ms, and a next-level computation about 6.60 mJ in 923 ms. Both are covered by the approximately 7.2 mJ harvested per actuation of the FMH array, ensuring uninterrupted operation without external power.

TABLE III
ENERGY CONSUMPTION AND PROCESSING TIME FOR VARIOUS GAME STATES

Process	Energy Consumed (mJ)	Processing Time (ms)
MCU Initialization	0.27	366
Checkpoint Resume	0.11	8
Single Step Computing	0.04	5
Next Level Computing	0.36	20
Checkpoint Save	0.28	19
E-ink Initialization	0.43	24
TX Data to E-ink	1.14	92
Local E-ink Refreshing	3.48	394
Global E-ink Refreshing	4.00	394
Total (Single Step)	5.75	908
Total (Next Level)	6.60	923

E. Interaction Evaluation

Fig. 11(a) demonstrates the practical operation process using the game prototype, where the user controls and moves a character toward a target position to clear the level. The synchronized waveforms are shown in Figs. 11(b)–(e): (b) regulator supply voltage; (c) charging voltage of the storage capacitor C_{sto}; (d) load current of the interaction unit (MCU and peripherals such as FRAM, button, and e-ink display); and (e) pressing forces over time at the four fingertips (index, middle, ring, and little), measured on the handpad using pressure-glove FSR sensors.

For the Input tolerance. During gameplay, execution is robust to pacing and force variations: presses at different tempos and with varying force levels all advance the game correctly, as shown in Figs. 11(c) and (e). Each press contributes a discrete energy increment that raises the storage-capacitor voltage; execution begins only after the operating threshold is reached, and below threshold the MCU and peripherals remain off. As a result, insufficient presses do not cause partial execution, whereas sufficiently energetic presses—whether fast or slow, strong or light—complete one atomic operation. To complete the picture across user pacing, the Supplementary Materials provide Movie S1 (fast/medium/slow interactions) and Figs. S6–S8. The synchronized waveforms and consistent voltage steps qualitatively show stable energy accumulation across tempos and threshold-gated task completion.

For the Output reliability. Across repeated evaluations, the harvested energy per press and the load-current envelopes during computation remained tightly bounded and repeatable, as shown in Figs. 11(b) and (d). The active-phase profiles and phase boundaries were consistent across trials, indicating stable and deterministic execution throughout the processing and display phases. Furthermore, the Supplementary Materials (Figs. S9–S11) validate cold-start reliability: when the interaction interval is approximately 310–900 ms, activations raise the storage-capacitor voltage above the operating threshold and the system completes a single atomic cycle. This behavior aligns with per-actuation mechanical energy buffering and task-aligned electrical energy release: no execution occurs below the threshold, and once crossed the task completes—confirming task-level sufficiency under both typical and cold-start pacing.

For the UI–data consistency. Transactional commits align one-to-one with the host-application logs and the oscilloscope timeline, yielding a consistent mapping from user presses to

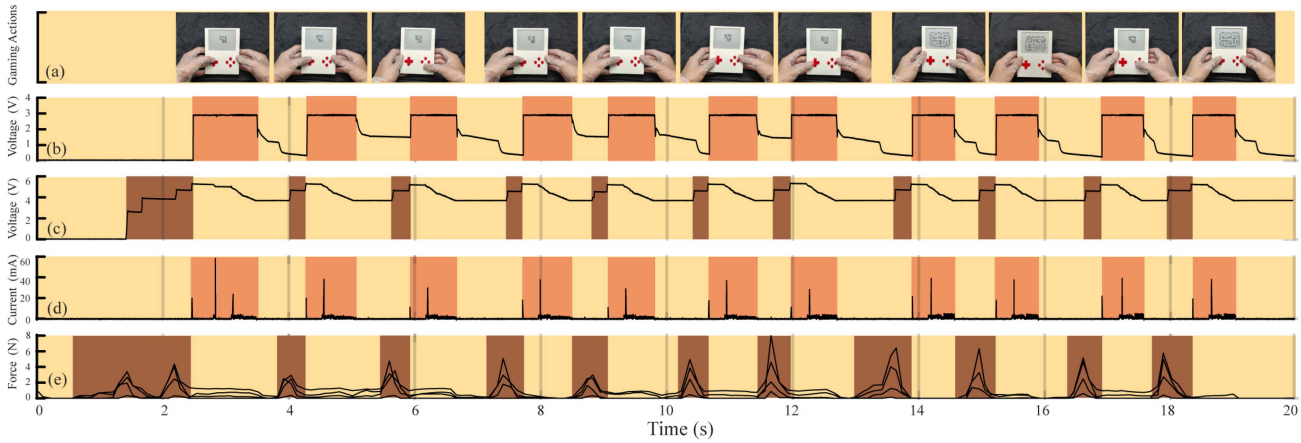

Fig. 11. Performance evaluation of the interactive quality of the FMH-game during gameplay. (a) Demonstration of the operation process and corresponding actions; (b) Regulator supply voltage; (c) Charging voltage of the storage capacitor (C_{sto}); (d) Current consumption of the load, including the MCU and peripherals such as FRAM, button, and e-ink display; (e) Hand-cap pressing force over time at four fingertips (index, middle, ring, and little) during gameplay. The colored rectangular blocks indicate operational phases along the gameplay timeline: brown denotes the fingertip actuation and energy-harvesting phase, orange denotes the game-execution phase, and yellow denotes idle intervals without active tasks.

state updates. In Figs. 11(a) and (e), each press (force peak) coincides with the start of an execution phase in the synchronized waveforms and with a corresponding commit event; the same correspondence holds under varied pacing. The supplementary movies illustrate this alignment: Movie S2 presents a representative interaction evaluation session with synchronized electrical and pressing force traces, while Movie S3 shows the complete interaction loop from user actuation to the final display update.

VI. Conclusion

This paper has presented a battery-free interactive gaming device powered entirely by energy harvested from fingertip motion. The proposed system integrates multiple elastically interconnected kinetic energy harvesting units with a bistable mechanical structure, effectively leveraging nonlinear dynamics and magnetic hysteresis to reliably convert subtle fingertip movements into electrical energy. Experimental results demonstrated stable and repeatable energy harvesting performance, consistently delivering 7.2–8.8 mJ per activation. Moreover, the synchronized triggering behavior of the energy harvesting units significantly enhanced instantaneous power output. An intermittent execution architecture was employed to support atomic game-task execution, enabling seamless interaction with minimal latency under fluctuating and intermittent energy conditions. Overall, this work provides a practical and effective solution for battery-free interactive systems, showcasing its broad potential in human–computer interfaces and energy-constrained sensing applications.

References

[1] Z. Lai, J. Xu, C. R. Bowen, and S. Zhou, "Self-powered and self-sensing devices based on human motion," *Joule*, vol. 6, no. 7, pp. 1501–1565, 2022.

[2] S. Khalid, I. Raouf, A. Khan, N. Kim, and H. S. Kim, "A review of human-powered energy harvesting for smart electronics: Recent progress and challenges," *Int. J. Precis. Eng. Manuf.-Green Technol.*, vol. 6, pp. 821–851, 2019.

[3] C.-Y. Sue and N.-C. Tsai, "Human powered mems-based energy harvest devices," *Appl. Energy*, vol. 93, pp. 390–403, 2012.

[4] W. Lin, Y. Wei, X. Wang, K. Zhai, and X. Ji, "Study on human motion energy harvesting devices: A review," *Machines*, vol. 11, no. 10, 2023, Art. no. 977.

[5] C. Zhang, Z. Lai, X. Rao, J. Zhang, and D. Yurchenko, "Energy harvesting from a novel contact-typedielectric elastomer generator," *Energy Convers. Manage.*, vol. 205, 2020, Art. no. 112351.

[6] H. J. Oh et al., "A highly porous nonwoven thermoplastic polyurethane/polypropylene-based triboelectric nanogenerator for energy harvesting by human walking," *Polymers*, vol. 12, no. 5, 2020 Art. no. 1044.

[7] F. Deng, Y. Cai, X. Fan, P. Gui, and J. Chen, "Pressure-type generator for harvesting mechanical energy from human gait," *Energy*, vol. 171, pp. 785–794, 2019.

[8] L. Xie and M. Cai, "An in-shoe harvester with motion magnification for scavenging energy from human foot strike," *IEEE/ASME Trans. Mechatron.*, vol. 20, no. 6, pp. 3264–3268, Dec. 2015.

[9] H. Lee and J.-S. Roh, "Wearable electromagnetic energy-harvesting textiles based on human walking," *Textile Res. J.*, vol. 89, no. 13, pp. 2532–2541, 2019.

[10] Y. Kuang, T. Ruan, Z. J. Chew, and M. Zhu, "Energy harvesting during human walking to power a wireless sensor node," *Sensors Actuators A: Phys.*, vol. 254, pp. 69–77, 2017.

[11] T. Xue, S. Williams, R. Rantz, M. A. Halim, and S. Roundy, "System modeling, characterization, and design considerations for generators in commercial watches with application to energy harvesting for wearables," *IEEE/ASME Trans. Mechatron.*, vol. 23, no. 5, pp. 2515–2524, Oct. 2018.

[12] A. George, D. Moline, and J. Wagner, "A mobile energy harvesting autowinder–build and test," *Renewable Energy*, vol. 146, pp. 2659–2667, 2020.

[13] M. Cai, J. Wang, and W.-H. Liao, "Self-powered smart watch and wristband enabled by embedded generator," *Appl. Energy*, vol. 263, 2020, Art. no. 114682.

[14] J. Chen et al., "Personalized keystroke dynamics for self-powered human–machine interfacing," *ACS Nano*, vol. 9, no. 1, pp. 105–116, 2015.

[15] S. Li et al., "All-elastomer-based triboelectric nanogenerator as a keyboard cover to harvest typing energy," *ACS Nano*, vol. 10, no. 8, pp. 7973–7981, 2016.

[16] P. Wang et al., "Complementary electromagnetic-triboelectric active sensor for detecting multiple mechanical triggering," *Adv. Funct. Mater.*, vol. 28, no. 11, 2018, Art. no. 1705808.

[17] P. Maharjan et al., "High-performance keyboard typing motion driven hybrid nanogenerator," *Nano Energy*, vol. 88, 2021, Art. no. 106232.

[18] K. Fan, H. Qu, Y. Wu, T. Wen, and F. Wang, "Design and development of a rotational energy harvester for ultralow frequency vibrations and irregular human motions," *Renewable Energy*, vol. 156, pp. 1028–1039, 2020.

[19] S.-Y. Teng, K. Wu, J. Chen, and P. Lopes, "Prolonging VR haptic experiences by harvesting kinetic energy from the user," in *Proc. Proc. 35th Annu. ACM Symp. User Interface Softw. Technol.*, 2022, pp. 1–18.

[20] A. A. Arabi, X. Wang, Y. Zhang, and J. Kim, "E3D: Harvesting energy from everyday kinetic interactions using 3 D printed attachment mechanisms," *Proc. ACM Interactive, Mobile, Wearable Ubiquitous Technol.*, vol. 7, no. 3, pp. 1–31, 2023.

[21] J. De Winkel, V. Kortbeek, J. Hester, and P. Pawełczak, "Battery-free game boy," *Proc. ACM Interactive, Mobile, Wearable Ubiquitous Technol.*, vol. 4, no. 3, pp. 1–34, 2020.

[22] J. LIANG, X. LI, and H. YANG, "Kinetic energy harvesting toward battery-free IoT: Fundamentals, co-design necessity and prospects," *ZTE Commun.*, vol. 19, no. 1, pp. 48–60, 2021.

[23] H. Rahmani et al., "Next-generation IoT devices: Sustainable ECO-friendly manufacturing, energy harvesting, and wireless connectivity," *IEEE J. Microw.*, vol. 3, no. 1, pp. 237–255, Jan. 2023.

[24] Z. Cai, Q. Chen, T. Shi, T. Zhu, K. Chen, and Y. Li, "Battery-free wireless sensor networks: A comprehensive survey," *IEEE Internet Things J.*, vol. 10, no. 6, pp. 5543–5570, Mar. 2023.

[25] M. A. Halim, M. H. Kabir, H. Cho, and J. Y. Park, "A frequency up-converted hybrid energy harvester using transverse impact-driven piezoelectric bimorph for human-limb motion," *Micromachines*, vol. 10, no. 10, 2019, Art. no. 701.

[26] D. Dai and J. Liu, "Hip-mounted electromagnetic generator to harvest energy from human motion," *Front. Energy*, vol. 8, pp. 173–181, 2014.

[27] J. M. Donelan, Q. Li, V. Naing, J. A. Hoffer, D. Weber, and A. D. Kuo, "Biomechanical energy harvesting: Generating electricity during walking with minimal user effort," *Science*, vol. 319, no. 5864, pp. 807–810, 2008.

[28] Q. Lu, G. Xia, M. Cai, X. Li, J. Cao, and W.-H. Liao, "An ultralow frequency energy harvester with an asymmetric-stiffness pendulum inspired by biological grooming behavior," *IEEE Internet Things J.*, vol. 11, no. 13, pp. 24222–24233, Jul. 2024.

[29] G. Xia et al., "Comprehensive investigation of a broadband wearable energy harvester using adaptive kinetic energy reallocation mechanism," *Mech. Syst. Signal Process.*, vol. 206, 2024, Art. no. 110907.

[30] T. Miyoshi, M. Adachi, K. Suzuki, Y. Liu, and Y. Suzuki, "Low-profile rotational electret generator using print circuit board for energy harvesting from arm swing," in *Proc. IEEE Micro Electro Mechan. Syst.*, 2018, pp. 230–232.

[31] P. Maharjan, T. Bhatta, M. S. Rasel, M. Salauddin, M. T. Rahman, and J. Y. Park, "High-performance cycloid inspired wearable electromagnetic energy harvester for scavenging human motion energy," *Appl. Energy*, vol. 256, 2019, Art. no. 113987.

[32] L. Lu, G. Hu, J. Liu, and B. Yang, "5G nb-IoT system integrated with high-performance fiber sensor inspired by cirrus and spider structures," *Adv. Sci.*, vol. 11, no. 18, 2024, Art. no. 2309894.

[33] P. Zhu et al., "Non-hand-worn, load-free VR hand rehabilitation system assisted by deep learning based on ionic hydrogel," *Nano Res.*, vol. 18, no. 4, 2025, Art. no. 94907301.

[34] F. Bambusi, F. Cerizzi, Y. Lee, and L. Mottola, "The case for approximate intermittent computing," in *Proc. 21st ACM/IEEE Int. Conf. Inf. Process. Sensor Netw.*, 2022, pp. 463–476.

[35] B. Islam, Y. Luo, and S. Nirjon, "Amalgamated intermittent computing systems," in *Proc. Proc. 8th ACM/IEEE Conf. Internet Things Des. Implementation*, 2023, pp. 184–196.